alloys

MDPI

Article

Critical Shape for the Growth of Grain Boundary Twin Embryos in Mg and Mg Alloys: Crystal Plasticity Modeling

Yanqing Su [1,*], M. Arul Kumar [2] and Irene J. Beyerlein [3,4]

[1] Department of Mechanical and Aerospace Engineering, Utah State University, Logan, UT 84322-4130, USA
[2] Materials Science and Technology Division, Los Alamos National Laboratory, Los Alamos, NM 87545, USA
[3] Department of Mechanical Engineering, University of California, Santa Barbara, CA 93106-5070, USA
[4] Materials Department, University of California, Santa Barbara, CA 93106-5050, USA
* Correspondence: yanqing.su@usu.edu

Abstract: Application of polycrystalline hexagonal close packed (HCP) metals in engineering designs has been constrained by their anisotropic responses due to twinning and limited plasticity. In deformation, twins most often initiate at grain boundaries (GBs), and thicken and propagate across the grain. In this work, the GB twin embryos in Mg and Mg alloys, and the conditions that influence their propagation are investigated. Using a micromechanical crystal plasticity model, the role of embryo shape on the driving forces prevailing at the embryo boundaries that could support its expansion is studied. The modeled embryos are either planar, extending more in the shear direction than normal to the twin plane, or equiaxed. Results show that the thinner the embryo, the greater the driving forces for both thickening and forward propagation. Alloys with low prismatic-to-basal critical resolved shear stress (CRSS) ratios promote embryo thickening and large CRSS values for the slip mode that primarily accommodates the twin shear encourage propagation. The neighboring grains with orientations that enable local accommodation of the embryo twin shear by pyramidal slip promote forward propagation but have little effect on thickening. When two like embryos lie along the same GB, their paired interaction promotes forward propagation but hinders thickening.

Keywords: deformation twinning; crystal plasticity; twin embryo; magnesium alloys

check for updates

Citation: Su, Y.; Arul Kumar, M.; Beyerlein, I.J. Critical Shape for the Growth of Grain Boundary Twin Embryos in Mg and Mg Alloys: Crystal Plasticity Modeling. *Alloys* **2022**, *1*, 212–231. https://doi.org/10.3390/alloys1020013

Academic Editor: Nikki Stanford

Received: 4 June 2022
Accepted: 30 August 2022
Published: 5 September 2022

Publisher's Note: MDPI stays neutral with regard to jurisdictional claims in published maps and institutional affiliations.

Copyright: © 2022 by the authors. Licensee MDPI, Basel, Switzerland. This article is an open access article distributed under the terms and conditions of the Creative Commons Attribution (CC BY) license (https://creativecommons.org/licenses/by/4.0/).

1. Introduction

Dislocation slip and deformation twinning are two main mechanisms in plastic deformation of metals. In hexagonal close packed (HCP) metals, plastic slip is limited and hence deformation twinning becomes the main plastic deformation mechanism [1–3]. Unlike plastic slip, which tends to be homogeneous over the crystals and is associated with relatively small amounts of lattice rotation and shear, twins usually attain heterogeneous lamellar shape with abrupt lattice rotation and large amounts of shear [4–6]. Deformation twinning significantly affects the deformation behavior [7–9], ductility [10,11], formability [12,13], and failure [14–16] of HCP metals.

Twins develop within grains over a series of three stages that span a broad range of length scales from the atomic to the grain scale [17]. Understanding all stages and their transitions is important for potentially controlling twinning for customized properties and performance. The process starts with the creation of an embryo (nucleation) at the atomic scale. In polycrystalline metals, twins are seen to most often emanate from the grain boundaries (GBs), where stress concentration and defects are present [18–21]. Following embryo formation is stage two, in which the embryo propagates into the interior of the grain taking the shape of a lamella. This stage begins with an atomic-scale embryo and usually ends with a high aspect ratio, nanoscale lamella that has fully crossed the grain and intersected with the GBs [22–26]. Twin propagation in this stage has been studied through in situ analyses as well as ex-situ analyses of twins that have terminated in the interior of the grain [4,6,27]. The final stage is thickening of the grain-scale lamella. The tips are often

stationary, pinned at GBs, while the coherent twin boundaries (CTBs) migrate by the glide of twinning dislocations [4,6,27–29]. The portion of the twin within the interior of the grain can experience faster growth rates than the pinned ends, giving the lamella an ellipsoidal shape [30,31]. Furthermore, multiple parallel, same variant twins and also non-parallel, different variant twins also formed, and significantly affect the mechanical response and microstructure evolution [32–35].

For several decades, extensive research efforts have been dedicated to understanding the first stage, twin nucleation, and the mechanisms at the atomic-scale [22,25,26,36–45]. From these studies, twin nucleation has been visualized as a sequential process of interaction of dislocation pile-ups with the defect structure at GBs, dissociation of GB dislocations into twinning dislocations (TDs) and then coalescence of these TDs to form a stable twin embryo [18,21,44–47]. The boundaries of small twin embryos are for the most part faceted, composed of basal-prismatic (BP), prismatic-basal (PB), or CTBs [22,36–38,48–50]. The PB boundary interfaces the $(1\bar{1}00)$ prismatic plane in the twin nucleus with the (0001) basal plane in matrix and the BP boundary, vice versa [22]. The formation of these boundaries has been rationalized as a shuffling mechanism [22] or using interfacial defect theory [36,37]. In Mg, the interplanar basal spacing is 5.21 Å and prismatic spacing 5.55 Å. In principle, advancing a PB in Mg requires a compression stress acting normal to its face and a BP boundary a normal tensile stress. The effects of solutes on this process have been recently probed via atomic scale simulation and post-mortem microscopy [51–53]. Compared to ordered twin boundaries, these facets have lower segregation energy [51,53]. In an experimental study of Mg-Y alloys, nanosize Y clusters were observed to preferentially form on PB and BP facets unlike at the CTBs in same alloy [52].

Many research studies have also focused on the third stage. The approaches taken range from atomistic simulation of the migration of a boundary to mesoscale phase field approaches for dynamics of boundaries and to micromechanical approaches that model the elastic and crystal plasticity response [21,54]. When provided a source for twinning dislocations (or disconnections), these defects can glide along the CTBs under a positive twin resolved shear stress (TRSS), changing the boundary location by its height. For the common $\{1\bar{1}02\}$ twin, atomistic simulations find the TD to be two planes high [21,55]. In alloys, atomistic simulations and microscopy analysis have shown that solutes can periodically decorate CTBs and hinder twin boundary migration [52,53,56,57]

Micromechanical approaches include discrete twin domains within crystals, permitting elastic anisotropic deformation, slip on crystallographic slip systems, and twin transformation strains. They have studied the expansion of the grain-scale lamella, and the strain and microstructural conditions required for the twin boundary migration [31,58–65]. For instance, such approaches have focused on the effect of grain neighbor orientation and its plastic response twin thickening. It was found that the effect of neighbor orientation arises from the slip systems it activated to locally accommodated the twin shear [63]. It could explain grain size effects as well as why some hcp materials promote thick twins while others thin ones [65]. In this type of approach, alloying effects are taken into account through the critical resolved shear stress (CRSS) values for the slip modes [66–68]. By affecting the local plastic response of the surrounding matrix and grains needed to accommodate the characteristic shear imposed by the twin, alloying controls the stresses at the twin boundary needed for propagation and growth [65]. At the mesoscale of such models, the effect of solutes on twinning were reflected by a change in the critical glide stress for TDs [69,70].

The less well-studied stage is the embryo expansion step within the second stage. Studies in this area have primarily utilized molecular dynamics (MD) simulation and/or in-situ transmission electron microscope (TEM). A number of joint atomistic simulation and experimental studies have suggested that before a twin nucleus at a GB can propagate into the grain interior, it needs to reach a critical size [21,25,71,72]. Producing a nucleus of critical size, approximately tens of nanometers in width, involves the coalescence of many tinier, nanometer size twin embryos. MD was employed to study the stress-driven expansion

of an embryo fully embedded in its parent crystal [24]. They found that TDs formed at the intersection of the CTB and PB boundaries and moved along the CTBs causing them to migrate. The growth of the embryo was anisotropic, with the PB/BP fronts moving outwards (propagation), extending its length in the twin shear direction, faster than the CTB migration (thickening) process. The effect of solutes on the propagation of embryo into a lamella is yet to be studied. Based on the prior atomistic and micromechanical studies on boundary migration, however, it can be anticipated that alloying would play an important role on the twin embryo expansion. Last, most twins emanate from GBs, and thus, similar to nucleation and growth, the neighbor orientation will likely influence the propagation of an embryo formed at GBs.

In this work, we employ a micromechanical full-field crystal plasticity fast Fourier transform (CP-FFT) model that accounts for the twin transformation strain within discrete twin domains [28] to study the transition from stage one to two in the twinning process; that is, when a twin embryo begins to expand into a lamella. The micromechanical technique is applied to calculate the stresses along the boundaries of a model embryo lying at a GB. For simplicity, the simulated crystalline microstructure is columnar and the embryo is represented by a parallelogram with two CTBs and a single PB twin front (TF). In all cases, the embryo is initially equiaxed or planar, extending from the GB into the parent crystal more than its thickness. We investigate the role of alloying, through its affect on CRSS for slip, and of the neighboring grain orientation. Based on the insight gained from the single embryo case, we perform simulations on a pair of embryos, in order to elucidate the effect of their spacing on their individual growth. The model suggests that alloying and grain neighbor orientation strongly influences the critical shape for either thickening (CTB migration) or propagation (PB advancement).

2. Methodology

2.1. CP-FFT Formulation for Explicit Crystallographic Twins

Based on the FFT framework proposed by Moulinec and Suquet [73], various CP-FFT models have been developed and employed to study crystalline materials, while considering different deformation modes, such as elasticity [74], incompressible visco-plasticity [75,76], dilatational visco-plasticity [77], infinitesimal elasto-visco-plasticity [78] and finite elasto-visco-plasticity [79]. Based on the infinitesimal elasto-visco-plastic FFT formulation of [78], Arul Kumar et al. [28] extended the CP-FFT model to account for the twin shear transformation within a preset twin domain. This formulation is used here and in this section, briefly reviewed.

The constitutive behavior of an elasto-visco-plastic material under an infinitesimal strain approximation with shear transformation is given by

$$\boldsymbol{\sigma}(\mathbf{x}) = \mathbf{C}(\mathbf{x}) : \boldsymbol{\epsilon}^{\mathrm{el}}(\mathbf{x}) = \mathbf{C}(\mathbf{x}) : \left(\boldsymbol{\epsilon} - \boldsymbol{\epsilon}^{\mathrm{pl}}(\mathbf{x}) - \boldsymbol{\epsilon}^{\mathrm{tr}}(\mathbf{x})\right) \tag{1}$$

where $\boldsymbol{\sigma}(\mathbf{x})$ is the Cauchy stress, $\mathbf{C}(\mathbf{x})$ is the elastic stiffness tensor, $\boldsymbol{\epsilon}^{\mathrm{el}}(\mathbf{x})$ is the elastic strain, $\boldsymbol{\epsilon}^{\mathrm{pl}}(\mathbf{x})$ is the plastic strain due to dislocation slip, and $\boldsymbol{\epsilon}^{\mathrm{tr}}$ is the transformation strain at a material point $\mathbf{x}$. $\boldsymbol{\epsilon}^{\mathrm{tr}}$ represents the shear transformation process of deformation twinning. The local stress field at each material point is calculated using an semi-implicit time discretization of the form:

$$\boldsymbol{\sigma}^{\mathrm{t}+\Delta\mathrm{t}(\mathbf{x})} = \mathbf{C}(\mathbf{x}) : \left(\boldsymbol{\epsilon}^{\mathrm{t}+\Delta\mathrm{t}} - \boldsymbol{\epsilon}^{\mathrm{pl,t}}(\mathbf{x}) - \dot{\boldsymbol{\epsilon}}^{\mathrm{pl},\mathrm{t}+\Delta\mathrm{t}}(\mathbf{x}, \boldsymbol{\sigma}^{\mathrm{t}+\Delta\mathrm{t}})\Delta t - \boldsymbol{\epsilon}^{\mathrm{tr,t}}(\mathbf{x}) - \Delta\boldsymbol{\epsilon}^{\mathrm{tr},\mathrm{t}+\Delta\mathrm{t}}(\mathbf{x})\right) \tag{2}$$

The plastic strain is assumed to be accommodated by dislocation slip. Accordingly the plastic strain-rate tensor $\dot{\boldsymbol{\epsilon}}^{\mathrm{pl}}$ is written as

$$\dot{\boldsymbol{\epsilon}}^{\mathrm{pl}}(\mathbf{x}) = \sum_{s=1}^{N^s} \mathbf{m}^s(\mathbf{x})\dot{\gamma}^s(\mathbf{x}) \tag{3}$$

where $\mathbf{m}^s$ is the Schmid tensor, $\dot{\gamma}^s$ is the shear rate, N^s is the total number of slip systems, the superscript 's' denotes a specific slip system, and

$$\dot{\gamma}^s(\mathbf{x}) = \dot{\gamma}_0 \left[\frac{|\mathbf{m}^s(\mathbf{x}) : \boldsymbol{\sigma}(\mathbf{x})|}{\tau_c^s(\mathbf{x})} \right]^{n_0} \times \text{sgn}[\mathbf{m}^s(\mathbf{x}) : \boldsymbol{\sigma}(\mathbf{x})] \tag{4}$$

$$\mathbf{m}^s(\mathbf{x}) = \frac{1}{2}[\mathbf{b}^s(\mathbf{x}) \otimes \mathbf{n}^s(\mathbf{x}) + \mathbf{n}^s(\mathbf{x}) \otimes \mathbf{b}^s(\mathbf{x})] \tag{5}$$

The multiplier $\dot{\gamma}_0$ is non-negative and controls the magnitude of $\boldsymbol{\epsilon}^{\text{pl}}$. Regarding the other parameters, n_0 is the stress exponent, τ_c^s is the CRSS, $\mathbf{b}^s$ is the Burgers vector, and $\mathbf{n}^s$ is the unit vector along slip plane normal.

For material points in the twin domain, the tensor $\boldsymbol{\epsilon}^{\text{tr}}$ is built up over several strain increments until the characteristic twinning shear strain T^{tw} is reached, i.e.,

$$\Delta\boldsymbol{\epsilon}^{\text{tr}}(\mathbf{x}) = \mathbf{m}^{\text{tw}}(\mathbf{x})\Delta\gamma^{\text{tw}}(\mathbf{x}) \tag{6}$$

where $\mathbf{m}^{\text{tw}}$ is the Schmid tensor associated with the twinning system, $\Delta\gamma^{\text{tw}}$ is the incremental shear strain, superscript 'tw' denotes a specific twinning system, and

$$\mathbf{m}^{\text{tw}}(\mathbf{x}) = \frac{1}{2}\left[\mathbf{b}^{\text{tw}}(\mathbf{x}) \otimes \mathbf{n}^{\text{tw}}(\mathbf{x}) + \mathbf{n}^{\text{tw}}(\mathbf{x}) \otimes \mathbf{b}^{\text{tw}}(\mathbf{x})\right] \tag{7}$$

$$\Delta\gamma^{\text{tw}}(\mathbf{x}) = \frac{T^{\text{tw}}(\mathbf{x})}{N^{\text{tw}}} \tag{8}$$

where $\mathbf{b}^{\text{tw}}$ is the unit vector along the twinning direction, $\mathbf{n}^{\text{tw}}$ is the unit vector along the twin plane normal, and N^{tw} is the number of increments to reach T^{tw}. Note that $\boldsymbol{\epsilon}^{\text{tr}}$ is non-zero only during the build-up of the twin transformation strain.

2.2. Model Set-Up

Figure 1 shows the bicrystal model unit cell containing GB twin embryos adopted for all calculations. The left crystal is a neighboring grain and the right crystal is the parent grain into which a twin embryo will expand. The parent orientation in Bunge convention is (0°, 0°, 0°), which aligns its c-axis with the z axis of the model unit cell. The simulated twin embryo variant is $(01\bar{1}2)[0\bar{1}11]$. The bicrystal microstructure is columnar extending through the thickness of the cell in x direction. The twin shear of this variant acts in plane (y-z plane). The twin embryo is L long and T thick.

The parent grain contains either a single twin embryo or two twin embryos. An embryo is modeled as a parallelogram with two CTBs inclined along the twin plane, a planar interface with the GB, and a single planar PB facet as the TF in the parent crystal, as illustrated in Figure 1a. The simulated twin embryo geometry is motivated by experimental and atomistic calculations. TEM-based experimental studies reveal that the twin nucleus in Mg is bounded by PB or BP facets [25,45]. Further, MD calculations suggest that the interaction of basal dislocations with GBs form several small twin embryos, and then they coalesce to develop a larger stable twin embryo with PB, BP, and CTBs as bounding interfaces [20,22,36,37]. The effect of the thickness of the twin embryo, T, is studied by varying the dimensionless ratio $t = T/L$ from 0.17 to 1 with the length of the twin embryo, L = 24 voxels. That is, the twin embryo thickness is varied from 4 voxels to 24 voxels. Note that we do not observe any noticeable Gibbs oscillations in the fields for these twin embryo configurations. Thus, the considered mesh sizes, i.e., twin embryo discretization, are sufficient to obtain the micromechanical fields correctly. The simulated thicknesses represent different stages of twin embryo expansion. For instance, $t = 1$ corresponds to an equisized stable twin embryo that has not yet propagated into the grain. On the other hand, $t < 1$ refers to the configurations where the twin embryo starts to propagate into the grains. In the two-embryo case, the influence of their spacing S, the distance between the lower CTB of the upper twin embryo (T1) and the upper CTB of the lower twin embryo (T2) along the z axis, is examined by varying the ratio $s = S/T$ from 0.5 to 8 (see Figure 1b). These

twin embryo spacings are consistent with the experimentally observed spacing between twin lamellae [4,23]. The simulation cell lengths are $0.125L$ (3 voxels), $21.2L$ (510 voxels), and $21.2L$ (510 voxels), along the x, y, and z directions, respectively. The simulation cell is encased by an outer layer (not shown) in the y-z plane with properties of a uniformly textured polycrystal to minimize periodic image forces. A thickness of 25 voxels is sufficient for this purpose and hence is used in all calculations that follow.

The twinning calculations are performed for both pure Mg and the alloys listed in Table 1. Three alloys are binary Mg-Y with three different Y wt.% and the fourth one is a Mg-0.47% Ca alloy. These binary alloy systems are selected such that the required crystal plasticity model parameters are already available. Furthermore, they were obtained using a similar modeling framework and constitutive law [69,70,80]. Further, these alloy systems are shown to exhibit excellent corrosion resistance and creep properties [81–85]. Thus, Mg-Y and Mg-Ca alloys are of great interest for several industrial applications, including the medical industry for bio-degradable implant material [86].

The model constitutive law requires elastic moduli, lattice parameters, and CRSS τ_c^s for three slip modes–basal $\langle a \rangle$, prismatic $\langle a \rangle$, and pyramidal $\langle c+a \rangle$ slip. The elastic moduli and lattice parameters for all alloys are set equal to those of pure Mg, under the assumption that they are not significantly altered by alloying [87,88]. The five independent elastic constants used are those measured for Mg at room temperature: $C_{11} = 59.75$ GPa, $C_{12} = 23.24$ GPa, $C_{13} = 21.7$ GPa, $C_{33} = 61.7$ GPa, and $C_{44} = 16.39$ GPa [87]. We model the effect of alloying on plastic response by using the τ_c^s values corresponding to each alloy. Note that these CRSS values account for an increase in the lattice friction for dislocation glide due to the presence of the solutes. Apart from this increase in the lattice friction, the alloying addition can potentially affect microstructure features via modulating the twin and GB migration. In this work, we focus on the driving stresses that could support twin embryo migration but not the kinetics of twin boundary migration. Thus, the effect of solutes on twin boundary migration is not accounted for. Further, the presence of solutes may govern the migration of GBs, and so the grain sizes. For example, the average grain size in Mg with 0.2% and 3.0% Y is 35.0 μm and 26.0 μm, respectively [69]. Since here we simulate a local region at the GB with twin embryos, the grain size reduction may not be relevant for the reported findings. For the calculation, we employ the τ_c^s values for the three slip modes, which have been characterized previously for these four alloys [69,70,80] and they are summarized in Table 1. In all alloys, basal slip is the easiest and the τ_c^s values for prismatic and pyramidal slip are relatively close compared to those of in pure Mg. These alloys are distinguished by their τ_0 value for basal slip, being hardest for the Mg-0.47% Ca alloy and easiest for Mg, and their ratio of hard $\langle c+a \rangle$ pyramidal slip to easy $\langle a \rangle$ basal slip, with Mg having the highest and the Mg-0.47% Ca alloy the lowest ratio.

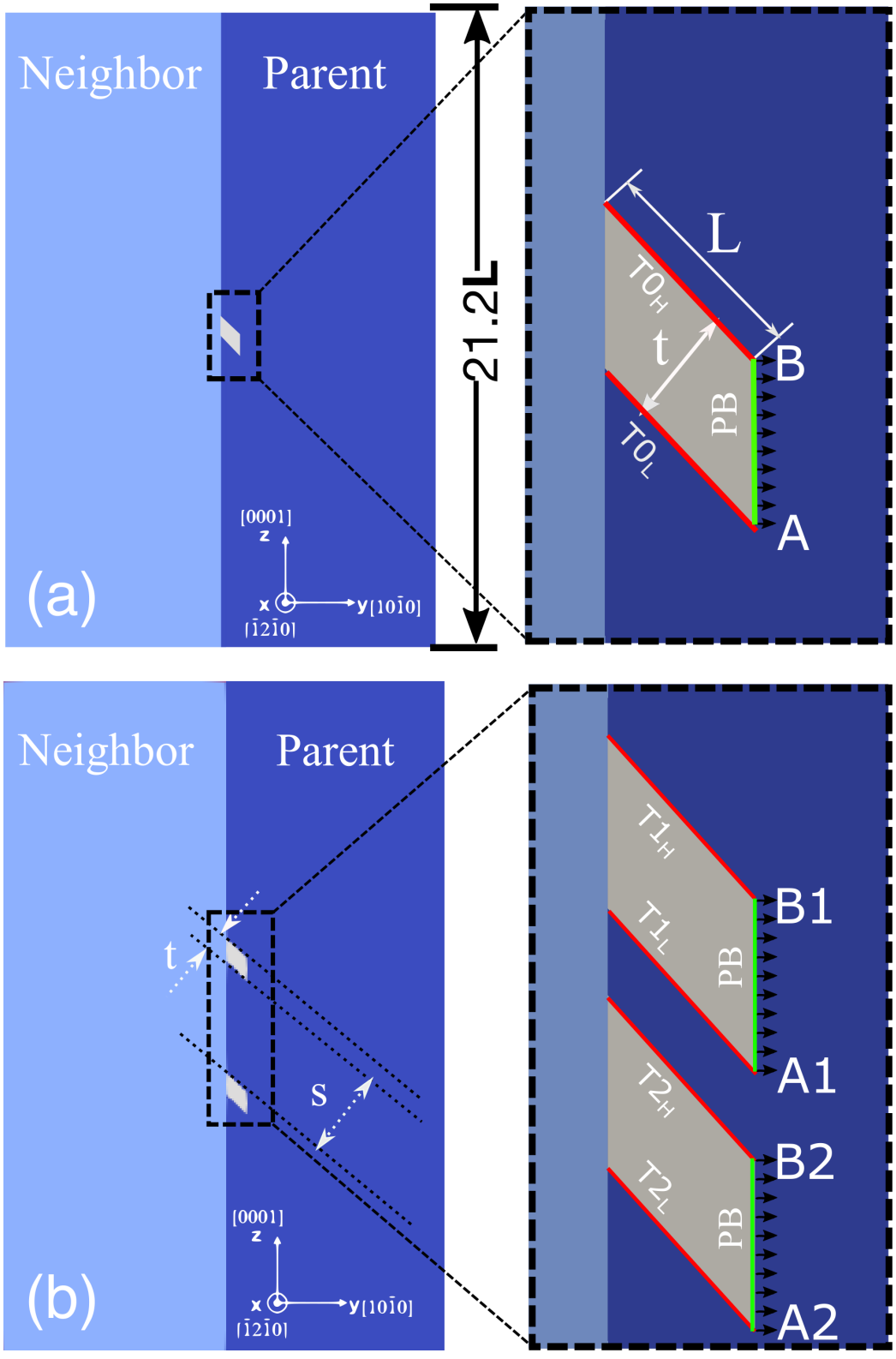

Figure 1. Schematic of the simulation cells containing (**a**) a single twin embryo and (**b**) two twin embryos. In both cases, the parent grain is oriented at (0°, 0°, 0°). Different neighboring grain orientations and twin embryo thicknesses T are studied. In the two-twin case, different twin embryo spacings S are studied.

The modeled embryos lie at a GB, and in the micromechanical simulation, the neighboring grain will be required to accommodate the twin shear. The local elastic and plastic

response of the neighbor will influence the stress fields generated around the embryo. For this reason, the calculations are repeated for a handful of neighboring grain orientations. Table 2 presents the crystallographic orientations of the neighboring grains considered. The list is not extensive, as the present focus lies on alloying effects. To select these, we aim to gain a rough idea of which slip mode is likely to contribute the most to accommodating the twin shear. For this, we employed the following geometric m' factor for a given slip system s in the neighboring grain [64]

$$m' = (\mathbf{b}_{\mathrm{t}} \cdot \mathbf{b}^{s}_{\mathrm{ne}})(\mathbf{n}_{\mathrm{t}} \cdot \mathbf{n}^{s}_{\mathrm{ne}}) \tag{9}$$

where subscripts 't' and 'ne' denote the simulated twin variant and neighboring grain, respectively, and $\mathbf{b}^s$ and $\mathbf{n}^s$ are the Burgers vector and plane for the slip system s in the neighboring grain. To calculate m', the slip systems in all three slip modes for Mg alloys are considered. Table 2 provides the slip system that leads to the maximum value of m' within a slip mode. As shown, the group of studied neighboring orientations represents two extreme ends–orientations that are either basal-slip or pyramidal-slip well-aligned to accommodate the twin shear. For an embryo fully embedded in its parent (C0) or joined to neighboring grain orientations C3 and C5, the accommodating slip mode would be pyramidal $\langle c + a \rangle$ slip. This is a relatively hard mode for all alloys and only in this respect, are these neighbors viewed to have "hard" orientations. The remaining neighboring grains are oriented such that basal $\langle a \rangle$ slip would mostly accommodates the twin shear and accordingly anticipated to be "soft" orientations. Note, however, that the CP-FFT calculations will predict the actual slip activity at the neighboring grain/embryo junction and m' is solely used to pre-select neighboring orientations.

Table 1. The CRSS, τ_c^s (MPa), for three slip modes in pure Mg [80], Mg-Y [69], and Mg-Ca [70].

Case	Basal	Prismatic	Pyramidal $\langle c + a \rangle$
Mg	3.3	35.7	86.2
Mg-0.2% Y	6	105	90
Mg-0.6% Y	9	85	100
Mg-1.0% Y	11	85	100
Mg-0.47% Ca	15	55	80

Table 2. Crystallographic orientations in the neighboring grain in Figure 1. The geometric measure m' for each slip system is defined in Equation (9).

Case	Euler Angles (in °)	m' (Basal)	m' (Prismatic)	m' (Pyramidal $\langle c + a \rangle$)
0	0,0,0	0.4609	0.2161	0.8651
1	75,62,0	0.8652	0.1528	0.5436
2	50,43,30	0.8866	0.2869	0.3914
3	0,90,0	0.4052	0.2161	0.8996
4	0,30,0	0.8212	0.0960	0.4191
5	0,100,0	0.2590	0.1983	0.9574

The micromechanical calculations for the stress fields are performed over a series of steps. First, a twin-free cell is subjected to a uniaxial compression of 0.1% strain along the y direction. Next, a twin embryo or embryos are introduced at the GB as pre-selected regions with a given shape L, T, and if applicable S. Under this compression state, the Schmid factor of the embryo tensile twin variant is 0.5. The embryo domain(s) are reoriented to the twin/matrix orientation relationship and the characteristic twin shear is built up slowly and relaxed at every time step. We use a small timestep size of 10^{-4} s and a large N^{tw} of 2000. Although not a limitation of the present formulation, the simulations here do not invoke strain hardening in τ_c^s and texture hardening, via plastic slip-induced lattice

re-orientations, for simplicity and to help focus on alloying effects through their marked differences in the initial τ_c^s.

From the full-field CP-FFT simulation, the spatially resolved complete stress and strain tensor, and slip activity are calculated. Of interest are the profiles of the driving forces along the three boundaries of the embryo interfacing with the surrounding parent matrix. The thickening of twin embryo by migrating the CTBs can be achieved by gliding of twinning dislocations, which is driven by the twin plane resolved shear stress (TRSS). Thus, the TRSS on the CTBs is calculated to study the driving force for embryo thickening. Similarly, the propagation of twin embryo by migrating the PB facet requires a favorable normal stress. As mentioned in Section 1, based on the separation between basal plane and prismatic plane, a compressive force is need to migrate PB facets. So, the normal stress on the PB twin front (TFNS) is calculated as the driving force for embryo propagation. These defects are unidirectional and a positive TRSS is required to move a positive TD and a negative (compressive) TFNS acting on PB boundary from the matrix is required to move the PB forward. In some cases, just in the post-analysis, we find it useful to arbitrarily assign a material twin critical glide shear stress (CGSS) and critical value for the TFNS, called CFNS, for TD and PB motion, respectively. A CGSS of 20 MPa and the TFNS equivalent to the CGSS, −40 MPa, are selected. We emphasize that these values are not used in the computation.

3. Results and Discussion

3.1. Single Twin Embryo in Mg and Mg Alloys

For reference, we first examine a single embryo in pure Mg. Using a representative planar embryo $t = 0.25$ and the C3 neighboring orientation for demonstration, Figure 2 presents typical TRSS/CGSS and TFNS/CFNS profiles. Along both the upper and lower CTBs, the TRSS varies from positive at the CTB/GB junction to negative (anti-twinning sense) over most of the CTB and back to positive near the end where the CTB and PB intersect. Due to the asymmetry of the embryo orientation relationship with the GB, the TRSS at the top and bottom CTBs are not the same. For the lower one, the TRSS acts in the twinning sense over a larger region than the upper one. Using the CGSS as a guide, we find that the TRSS exceeds the CGSS in two regions in the upper CTB (locally at the GB and at the CTB/PB intersection) and in one region in the lower one (at the CTB/PB intersection). The peak TRSS is, however, larger at the bottom CTB/PB junction.

The calculations find that due to the constraint from the GB and surrounding parent crystal, the TRSS is not constant along the CTB. A positive TRSS of sufficient intensity is presumed here to indicate an opportunity for thickening. We do not directly model the formation and glide of TDs nor do we consider how and when they form. This subject has been addressed but still remains to be clarified. In MD simulations of isolated embryos under deformation, TDs are seen to form at CTB/PB intersections or when lattice dislocation impinges on the CTBs [21,24], an observation that is consistent with stress fields from the present work. In simulations of planar CTBs under deformation, a dipole comprising a positive and negative TD have also been seen or proposed to form on the CTB [89,90]. The role of dislocation reactions on twin boundary migration seen in MD has been questioned and with micromechanical modeling it was argued that TD formation and glide from the GB junction was more likely than from lattice dislocation impingement [6]. The present micromechanical stress calculations here identify peak stresses that could locally push a positive TD from the GB junction along the CTB towards the interior or a negative TD at the the CTB/PB site towards the GB. Because of the anti-twinning region formed along the CTB, formation of the TD is anticipated to be easier than propagation. This notion is consistent with the observations of embryo growth in MD simulations [24,91].

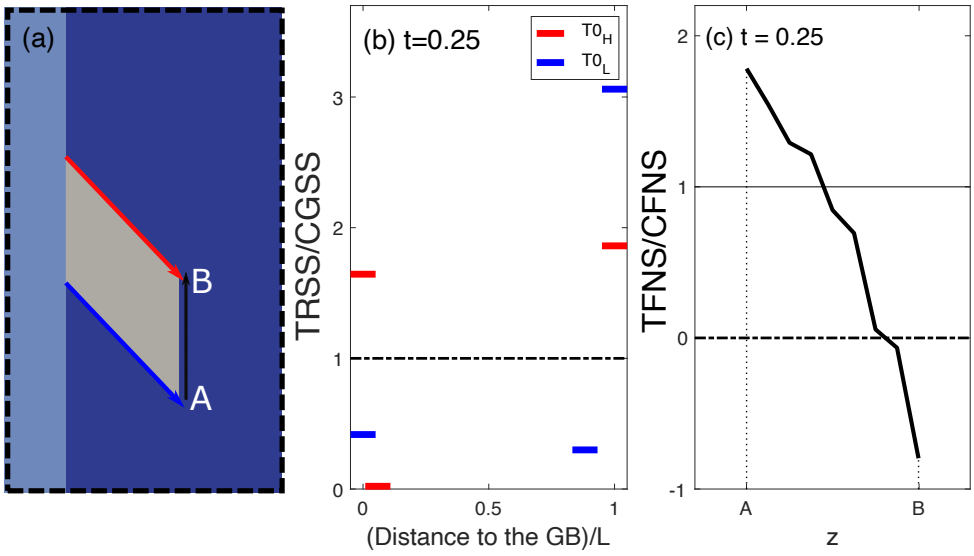

Figure 2. (**a**) The red (top CTB), blue (lower CTB), and black (BP) lines indicate the horizontal axes in (**b**,**c**) used by the lines in the same colors. (**b**) Profiles of TRSS along the upper and lower twin boundary $T0_H$ and $T0_L$ (Figure 1a) in the single twin embryo. The neighboring orientation is C3 (Table 2). Indicated by the red and blue arrows shown in (**b**), the profiles start at the GB, extend along the CTBs, and end at the CTB/PB intersection. The location of the GB and the TF are indicated by a solid and a dashed vertical line, respectively. The TRSS is normalized by the CGSS (20 MPa). The x-axis is the distance to the GB normalized by the length L of the twin embryo. (**c**) Profiles of TFNS (black curve) along the TF shown in (**b**). The TFNS values are normalized by CFNS $= -40$ MPa, the uniaxial stress corresponding to CGSS $= 20$ MPa.

The TFNS/CFNS profiles from A to B along the PB boundary are presented in Figure 2b,c. The traction is non-uniform across the front. A compressive stress (where TFNS/CFNS > 0) that could propagate the embryo forward develops in the lower half of the PB front. The peak TFNS is reached at the lower CTB/PB intersection and with all else being the same, implies that propagation is likely to initiate there. In the case CFNS $= -40$ MPa (TFNS/CFNS > 1), for instance, any portion of the lower third of the front could propagate.

The effect of embryo shape on these boundary stresses is investigated by varying t from 0.17 to 1. Over this t range the embryo is either planar, extending into the crystal more than its thickness or nearly equi-axed. These calculations are repeated for an embryo fully embedded in its parent crystal (C0) or the five other neighboring orientations listed in Table 2. For all t, the forms of the TRSS and TFNS profiles are the same as in Figure 2, but the peak values change. Figure 3a presents the variation in the peak TRSS. A strong shape effect is seen, with decreasing TRSS for thicker embryo. This result is insensitive to neighboring grain orientation. If CGSS is set to 20 MPa (or higher), the critical t above which CTB migration is unlikely is 0.4 (or lower).

Figure 3b shows the peak (compressive) TFNS along the PB front. As in the TRSS, a strong size effect is also seen in the peak TFNS, where a thicker embryo is less likely to propagate forward. As the embryo thickens from a thin lamella to a thickness-to-length aspect ratio of 0.5, the driving force decreases. A significant observation is the sensitivity to neighbor orientation. For the parent grain and two hardest orientations, the TFNS remains compressive and more prone to propagation. For the three other softer neighboring orientations, the peak TFNS becomes tensile, even for a thin embryo, $t \geq 0.2$, shutting down the chance for propagation. These soft neighbor orientations locally accommodate the twin shear primarily by basal slip system, the easiest slip system, and reducing the backstress that develops back onto the embryo from the resistance of the neighboring grain. The TFNS and the peak TRSS at the GB/twin intersection (not shown) are consequently

lower for these three basal-slip accommodating orientations compared to the pyramidal-slip accommodating ones (C3 and C5), while only a small group of neighbor orientations are tested, there is clearly a chance that propagation can be suppressed from lack of driving force due to a soft, plastically accommodating neighbor orientation.

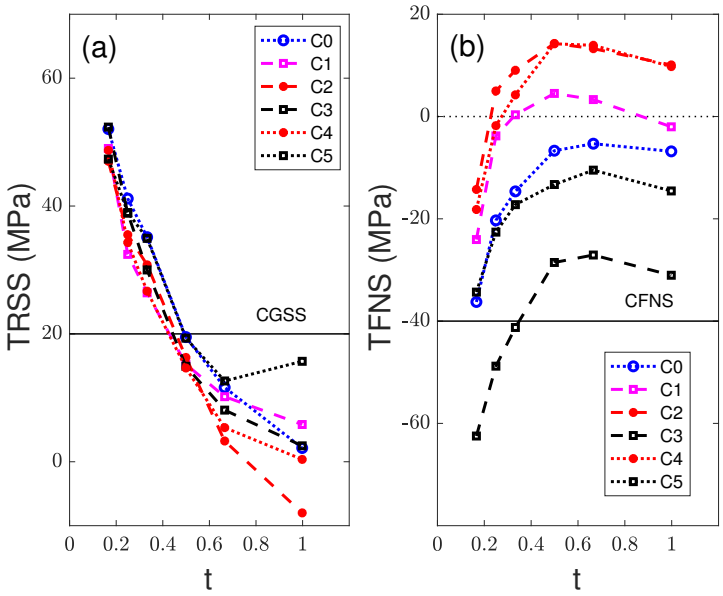

Figure 3. (**a**) TRSS and (**b**) TFNS corresponding to where the TRSS/CGSS and TFNS/CFNS reach a peak value as a function of t and for grain neighbor orientations C0–C5 in Table 2.

The variation in the peak TRSS and TFNS with t for different alloys are presented in Figure 4 ("soft" neighbor C4) and Figure 5 ("hard" neighbor C3). In the study of pure Mg, hard neighbor orientations tend to promote forward propagation while soft ones do not. The alloy calculations are performed for one of the soft (C4) and hard neighbor orientations (C3). From Figures 4a and 5a, we observe that compared to pure Mg, alloying can increase the drive for embryo thickening. For guidance, the CGSS values found previously for each alloy [69,70] are indicated. The more heavily alloyed the material, the lower the prismatic-to-basal τ_c^s ratio is. For the embryo, this reduction has the effect of increasing the peak TRSS and twin thickening. As for pure Mg changing the neighbor orientation from soft to hard for the alloys had negligible effect on the peak TRSS.

Figures 4b and 5b show the corresponding variation in peak TFNS. As expected from the pure Mg case, soft neighbor orientations generally hinder forward propagation compared to hard ones in the alloys. For the soft neighbor (Figure 4), the peak TFNS is seen insensitive to alloy composition, with the exception of the dilute Ca alloy. Employing the m' factor as a measure, soft alloys are classified as those that accommodate the twin shear locally by activating basal slip. This alloy had the highest basal τ_c^s. Nonetheless, the peak TFNS values are tensile for all alloys and would not enable forward propagation of the embryo. In contrast, as shown in Figure 5b, the hard neighbor generates compressive peak TFNS in every alloy studied. Hard neighbors are defined here as those that promote $\langle c+a \rangle$ activity towards accommodation. The results identify those alloys that enhance the pyramidal τ_c^s generate the large peak TFNS/CFNS values that could drive propagation. Although a full sweep of alloy types and neighbor orientations was not tested, the present results hint that the impact of alloying depends on neighbor orientation. Alloying that increases the resistance of the slip mode that chiefly acts to accommodate the twin shear facilitates propagating the embryo forward into the crystal.

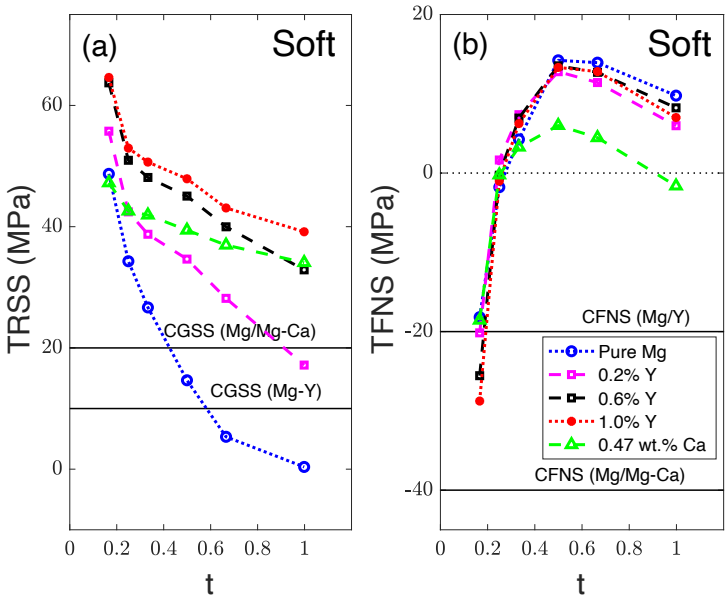

Figure 4. (**a**) TRSS and (**b**) TFNS where TRSS/CGSS and TFNS/CFNS achieve a maximum for pure Mg, Mg-Y, and Mg-Ca in C4 ("soft" neighbor). CGSS values are taken from Refs. [69,70,80].

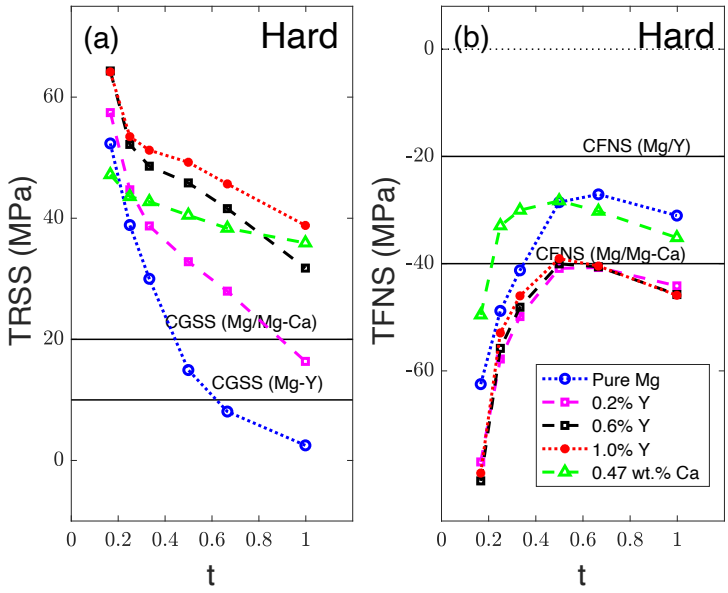

Figure 5. (**a**) TRSS and (**b**) TFNS where TRSS/CGSS and TFNS/CFNS achieve a maximum for pure Mg, Mg-Y, and Mg-Ca in C3 ("hard" neighbor). CGSS values are taken from Refs. [69,70,80].

3.2. Two Twin Embryos

We also preformed simulations on two like embryos separated by s along the GB. A relatively "soft" neighbor orientation (C2) and "hard" neighbor orientation (C3) are selected and hereinafter referred to as the soft and hard neighbors, respectively. For comparison with the single embryo cases, these embryos are also planar in shape, protruding into the crystal at a greater distance than their thickness.

Figure 6 considers two closely spaced embryos, $s = 0.5$, and studies the effect of their thickness t, by varying t from 0.17 to 1, on the TFNS. For comparison, the TRSS/CGSS profile for the single embryo with the same t in each case is included. The striking results are the asymmetry and suppression for propagation relative to the isolated embryo. For the range of t, the lower twin (T2) has the higher peak TFNS/CFNS than upper one (T1) and it occurs at its bottom CTB/PB intersection. The interactions between the embryos cause the

lower twin (T2) to become more likely to propagate forward relative to the upper one (T1). Their differences reduce as t increases above 0.7 and their TFNS distributions are nearly equal when the embryos are equiaxed.

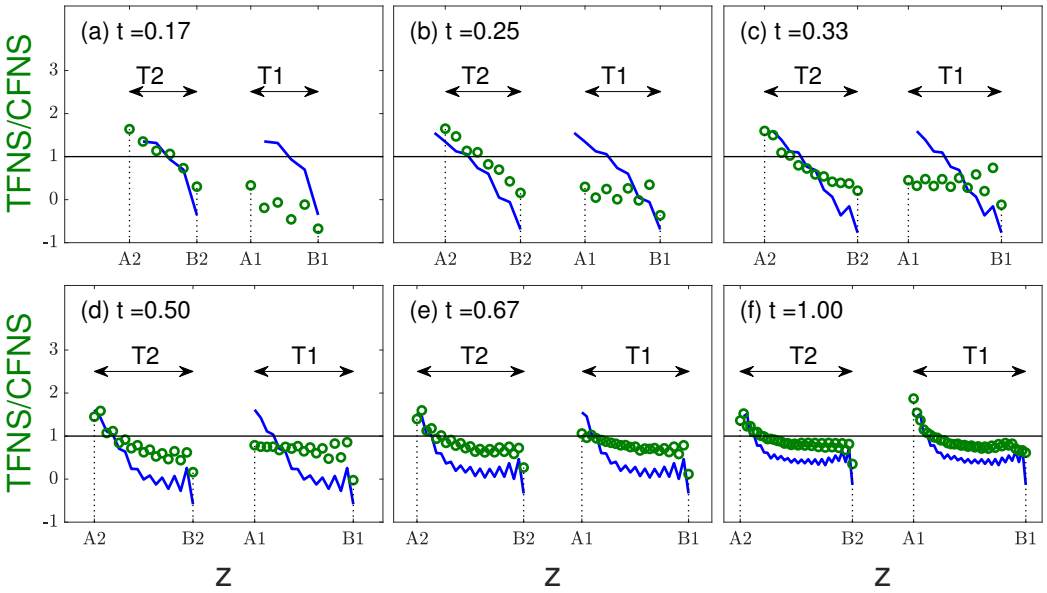

Figure 6. TFNS profile along the PB front for T1 and T2 as the thickness, t, varies from 0.17 to 0.67. The neighboring grain orientation is C3 and a spacing $s = 0.5$. The blue curves are the TFNS/CFNS profiles of the single embryo with the same thickness t.

The effects of their strong interactions on the TFNS are expected to decrease as s increases from 0.5. Figure 7 investigates the influence of s on the TFNS/CFNS distributions along the PB front, for a pair of moderately thin embryos $t = 0.5$ by increasing their s from 0.5 to 5. To elucidate the effect of their paired interaction, the TFNS/CFNS profile of the single embryo with the same $t = 0.5$ is overlaid on each profile. The important result to note is that for $s \geq 1$, the TFNS/CFNS ratio reaches a peak at the CTB/PB intersection on the PB front of both twins. The upper twin T1 has the slightly higher peak. As their s increases (approaching just two times their thickness in this particular case), their profiles become similar. As expected, when s increases even further, the distributions approach that of the single embryo although within the range of s studied, do not achieve it.

With interest in propagation, we observe that the peak TFNS/CFNS that could support propagation occurs at the lower CTB/PB intersections of both embryos and is for the most part not that different from the maximum in the isolated embryo case. To closely examine the differences in the peak TFNS/CFNS between these two embryos, Figure 8 shows the variation in peak TFNS/CFNS at all four CTB/PB junctions as a function of s. For all s, the peak TFNS is compressive. Significantly with the exception of the closest spacing $s = 0.5$, the peak TFNS intensity is greater at all four CTB/PB intersections than those for a single embryo. The interaction of the two embryos promotes forward propagation.

For the same cases, Figure 9 shows the corresponding peak TRSS values that develop on all four CTBs, the upper and lower boundaries of the top embryo T1 and the bottom embryo T2. For the range of s, the interactions between the embryos cause the upper twin (T1) to become more likely to thicken relative to the lower one (T2). This upper twin has the higher peak TRSS and likely to thicken from its upper boundary, the one furthest away from the lower twin. This driving force is insensitive to s and it is nearly equal to its peak when it was an isolated embryo. For closely spaced embryos, growth of T2 is suppressed. However, for separations as small as $s = 2$ (and also greater), the effects of their interaction already weaken and hence thickening of T2 is possible.

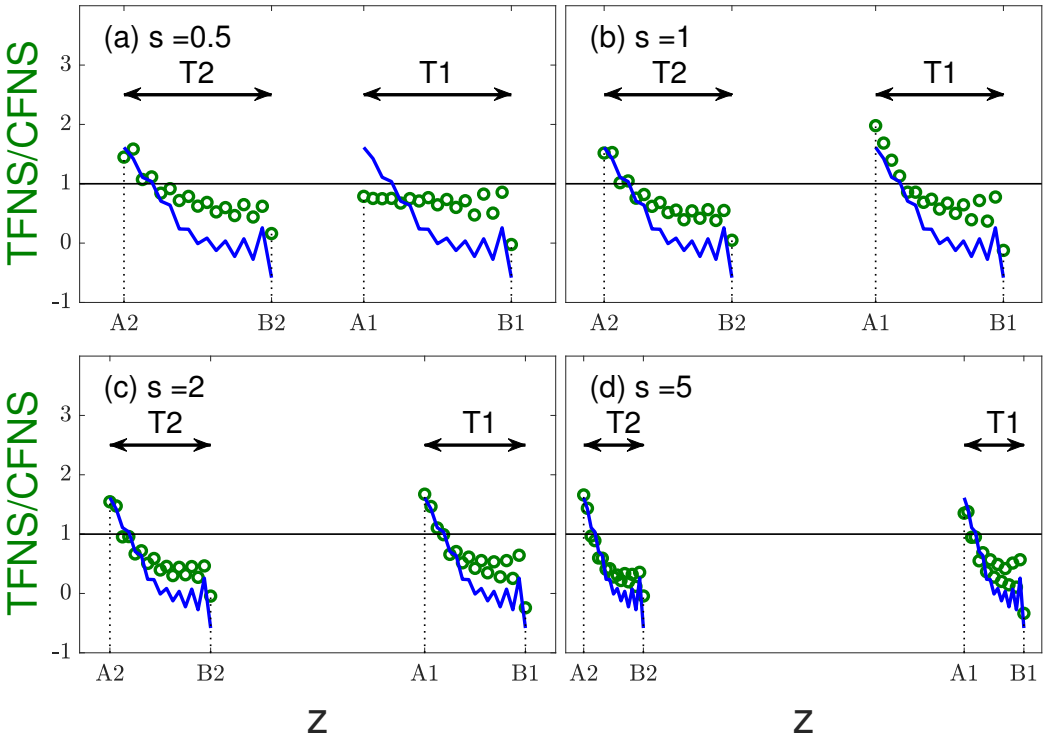

Figure 7. TFNS/CFNS profile along the PB front of the two twin embryos as the spacing s varies from 0.5 to 5. The neighboring grain orientation is C3 (see Table 2) and the normalized twin embryo thickness t is 0.5. The blue curves are the TFNS/CFNS profiles of the single embryo with $t = 0.5$.

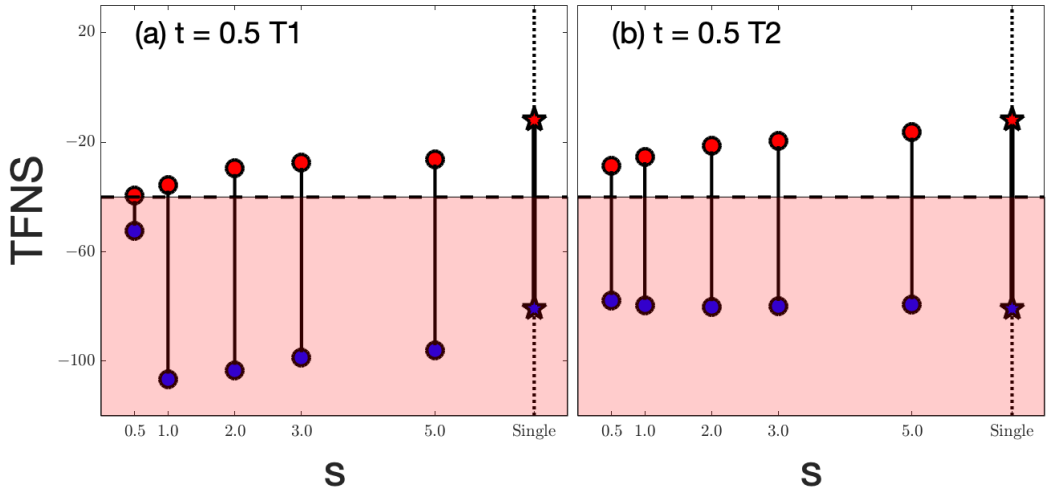

Figure 8. The peak TFNS/CFNS obtained from Figure 7 with red symbols representing the upper CTB/PB intersection of each embryo (B1 or B2 in Figure 1b) and blue symbols for the lower intersection one (A1 or A2 in Figure 1b). The shaded region indicates areas with TFNS/CFNS > 1. (**a**) T1 (upper twin embryo) and (**b**) T2 (lower twin embryo) in Figure 1b. The red and blue stars are the single twin embryo results at upper (B) and lower (A) CTB/PB intersections, respectively, as indicated in Figure 1a.

Since both s and t can influence the local stresses relevant for thickening and propagation, we plot the peak driving forces on s and t axes in Figure 10 (map of TRSS) and Figure 11 (map of TFNS). Figure 10 presents the peak TRSS in the upper CTB of T1 for a soft and hard neighbor orientations. The map identifies that for most s, thickening is possible when the embryos are thin, $t \leq 0.4$. It also reveals that closely spaced embryos can promote thickening, particularly when the neighboring orientation is plastically hard.

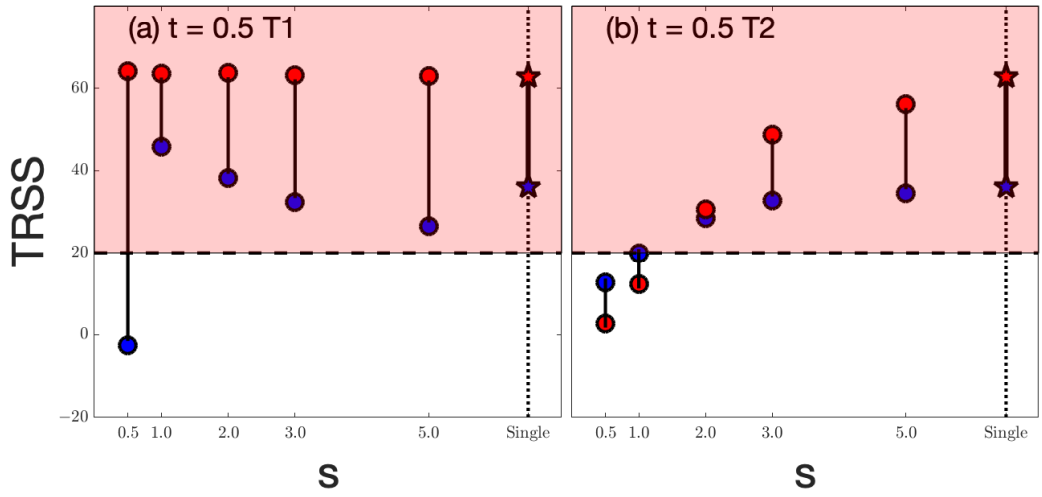

Figure 9. Peak TRSS for $t = 0.5$ for various s. Red symbols represent the upper CTB for each of the twin embryos and blue the lower one. The shaded region indicates areas with TRSS>CGSS. (**a**) T1 (upper twin embryo) and (**b**) T2 (lower twin embryo) in Figure 1b. The red and blue stars correspond to the single twin embryo case.

The maps in Figure 11 of the TFNS corresponding to the peak TFNS/CFNS on the upper twin (T1) show regions in t-s space that would potentially lead to propagation. The soft neighbor nearly suppresses all chances for propagation. Over most of the space, the TFNS is tensile. Compressive TFNS that can trigger propagation only develops for large s and either very thin t or $t \approx 0.5$. In stark contrast, for a hard neighbor, the peak TFNS/CFNS is compressive over most of the space. For close spacings, $s \leq 2$, propagation is possible for nearly all t. For larger s, the embryos need to be thinner, $t \leq 0.6$.

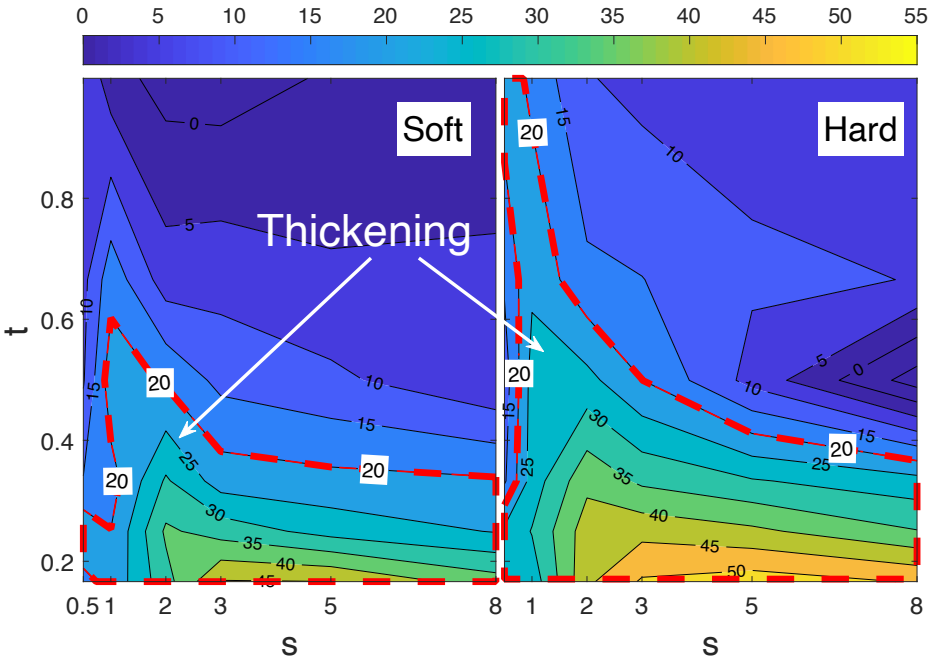

Figure 10. Map of the peak TRSS along the CTB of T1 in the two twin embryo system for the soft (C2) and hard (C3) neighbor for combinations of t from 0.17 to 1 and s from 0.5 to 8. Areas where TRSS exceeds the CGSS are delineated by a red dashed line.

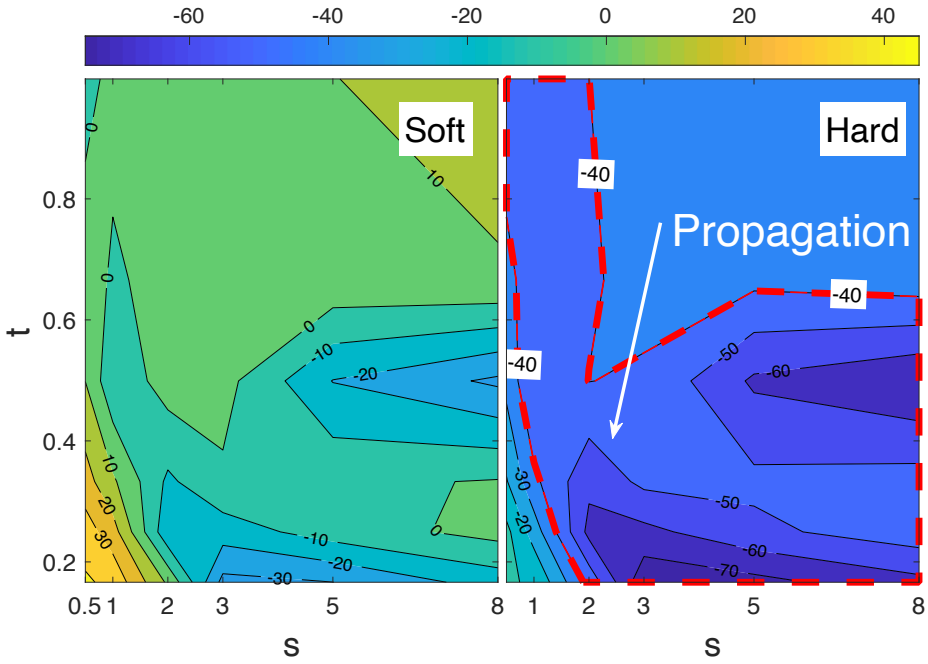

Figure 11. Map of the TFNS corresponding to the peak TFNS/CFNS along the PB front of T1 in the two twin embryo systems for the soft (C2) and hard (C3) neighbor for combinations of t from 0.17 to 1 and s from 0.5 to 8. Areas where TFNS lower than -40 MPa are delineated by a red dashed line.

4. Discussion

The present study focuses on stresses along boundaries of an embryo of a given shape and not on the dynamics of boundary motion. The relative mobilities of these two boundaries under these stresses would depend on material properties, such as the mobilities of TDs on CTBs and PB facets for the $\{10\bar{1}2\}$ twin and the effect of alloying elements [51]. However the calculations could provide direct insight in the event that differences between TD and PB formation energies and mobilities are small. Comparison of the extent of favorable driving forces would suggest that the propagation of its PB front is more likely than migration of its CTB. Unequal driving forces for migration vs. propagation may also explain the wedge-like shape of twin embryos protruding from GBs [25,92]. When the TF propagates forward, away from the GB, its length-to-thickness ratio increases. This shape change increases the peak TRSS along its CTBs, increasing the chances for CTB migration. If it were to consequently thicken, its length to thickness ratio would decrease and so will the intensity of the TRSS. With the drive to continuing thickening reduced, the embryo would need to propagate forward at its front. This sequence of crystallographic boundary migrations could lead to an embryo that is finer at its tip than the length it overlaps with its originating GB.

Alloying affects the τ_c^s values among the preferred slip systems [12]. With the few choice alloys tested, the analysis points to alloys with low prismatic-to-basal τ_c^s ratio for promoting embryo thickening and high τ_c^s values for the accommodating slip mode for forward propagation. Oftentimes multiple fine twin lamellae are desired for hardening the grain. This twin structure can be realized by adjusting alloying to ease the activation of pyramidal slip and enable embryos to grow into the crystal as thin lamellae.

Although all studied embryos are planar or equiaxed, i.e., $t \leq 1$, the results could give insight into the case of super thick embryos, i.e., $t > 1$. For the planar embryos here, TRSS increases as the distance between its CTB/PB and the GB increases. This result would imply that in the case of very thick embryos, elongated along the GB more so than they protrude into the crystal, would not thicken. For such large t, the key question could then concern the critical shape that would enable the embryo front to propagate forward. The study of stress states along the PB front here would suggest that propagation of such thick embryo

would be sensitive to the orientation of the neighbor grain. In fact, the peak TFNS becomes compressive for larger t beyond ≈ 0.6. This trend could indicate that embryos with very large t could develop compressive TFNS values that would drive propagation.

Figure 9 would imply that the stress state does not favor merging of the two closely spaced twin embryos. For the pair to merge, we would look for sufficient driving forces for the migration of the two inner CTBs ($T1_L$ and $T2_H$ in Figure 1b) towards each other. As s reduces to 0.5, the TRSS on these two inner CTBs $T1_L$ (indicated by the blue dots in Figure 9a) and $T2_H$ (indicated by the red dots in Figure 9b) is nearly zero or negative (anti-twinning).

5. Conclusions

In this work, we study the role of twin embryo shape on the stresses that would be responsible for moving its twin boundaries from a GB into its parent crystal. The embryo lies at a GB, is a $\{10\bar{1}2\}$ twin, and belongs to Mg or an Mg alloy. Using CP-FFT adapted for discrete twin lamellae, we investigate the role of alloying as well as orientation of the neighboring grain. For simplicity, the model crystalline microstructure is columnar with the twin variant and its twin shear lies within a plane. The embryo is represented as a parallelogram with two CTBs that can migrate, thickening the twin, a stationary interface with the GB, and a single PB TF that can move forward propagating the embryo. The TRSS on the CTBs is calculated to study the driving force for embryo thickening. Likewise, TFNS is calculated to analyze the driving force for embryo propagation. Based on the insight gained from the single embryo case, we perform simulations on a pair of embryos, in order to elucidate the effect of their spacing on their individual growth. Key results are as follows:

1. The TRSS that could drive CTB migration develop at the CTB/GB and CTB/PB intersections. The larger the aspect ratio (length to thickness) of the embryo, the greater is the intensity.
2. The compressive normal stress that could propagate the PB front into the parent crystal intensifies as the aspect ratio increases.
3. Thickening is promoted in alloys with low prismatic–to–basal CRSS ratio and propagation of the embryo into the parent grain is encouraged in alloys with high CRSS for the slip mode that accommodates the twin shear.
4. The peak TFNS for forward propagation is strongly influenced by neighbor orientation, increasing for grain neighbors well suited to accommodate the twin shear via pyramidal slip, the hardest slip mode. Thickening is relatively insensitive to grain neighbor orientation.
5. For a pair of embryos, thickening would occur unevenly, being preferred in one of the outer CTBs but not both. This result is insensitive to their spacing and neighbor orientation.
6. With the exception of the closest spacing $s = 0.5L$, where L is the embryo length, the peak TFNS intensity is greater at all four CTB/PB intersections than those for a single embryo. The interaction of the two embryos promotes forward propagation.

Author Contributions: Conceptualization, I.J.B. and M.A.K.; methodology, Y.S. and M.A.K.; software, M.A.K.; formal analysis, Y.S.; investigation, Y.S.; writing—original draft preparation, Y.S.; writing—review and editing, Y.S., I.J.B. and M.A.K.; visualization, Y.S.; supervision, I.J.B.; funding acquisition, I.J.B. and M.A.K. All authors have read and agreed to the published version of the manuscript.

Funding: Y.S. and I.J.B. acknowledge financial support from the National Science Foundation (NSF MOM-2051390). M.A.K. acknowledges financial support from the US Department of Energy, Office of Basic Energy Sciences (OBES) FWP-06SCPE401.

Data Availability Statement: Not applicable.

Acknowledgments: Use was made of computational facilities purchased with funds from the National Science Foundation (CNS-1725797) and administered by the Center for Scientific Computing (CSC). The CSC is supported by the California NanoSystems Institute and the Materials Research Science and Engineering Center (MRSEC; NSF DMR 1720256) at UC Santa Barbara.

Conflicts of Interest: The authors declare no conflict of interest.

References

1. Partridge, P.G. The crystallography and deformation modes of hexagonal close-packed metals. *Metall. Rev.* **1967**, *12*, 169–194. [CrossRef]
2. Yoo, M.H. Slip, twinning, and fracture in hexagonal close-packed metals. *Metall. Trans. A* **1981**, *12*, 409–418. [CrossRef]
3. Yoo, M.H.; Lee, J.K. Deformation twinning in h.c.p. metals and alloys. *Philos. Mag. A* **1991**, *63*, 987–1000. [CrossRef]
4. Beyerlein, I.J.; Capolungo, L.; Marshall, P.E.; McCabe, R.J.; Tomé, C.N. Statistical analyses of deformation twinning in magnesium. *Philos. Mag.* **2010**, *90*, 2161–2190. [CrossRef]
5. Beyerlein, I.J.; Zhang, X.; Misra, A. Growth twins and deformation twins in metals. *Ann. Rev. Mater. Res.* **2014**, *44*, 329–363. [CrossRef]
6. Capolungo, L.; Marshall, P.E.; McCabe, R.J.; Beyerlein, I.J.; Tomé, C.N. Nucleation and growth of twins in Zr: A statistical study. *Acta Mater.* **2009**, *57*, 6047–6056. [CrossRef]
7. Proust, G.; Tomé, C.N.; Jain, A.; Agnew, S.R. Modeling the effect of twinning and detwinning during strain-path changes of magnesium alloy AZ31. *Int. J. Plast.* **2009**, *25*, 861–880. [CrossRef]
8. Salem, A.A.; Kalidindi, S.R.; Doherty, R.D.; Semiatin, S.L. Strain hardening due to deformation twinning in α-titanium: Mechanisms. *Metall. Mater. Trans. A* **2006**, *37*, 259–268. [CrossRef]
9. Wroński, M.; Kumar, M.; Capolungo, L.; McCabe, R.; Wierzbanowski, K.; Tomé, C. Deformation behavior of CP-titanium: Experiment and crystal plasticity modeling. *Mater. Sci. Eng. A* **2018**, *724*, 289–297. [CrossRef]
10. Barnett, M.R. Twinning and the ductility of magnesium alloys: Part I: "Tension" twins. *Mater. Sci. Eng. A* **2007**, *464*, 1–7. [CrossRef]
11. Barnett, M.R. Twinning and the ductility of magnesium alloys: Part II. "Contraction" twins. *Mater. Sci. Eng. A* **2007**, *464*, 8–16. [CrossRef]
12. Kumar, M.A.; Beyerlein, I.J.; Tomé, C.N. A measure of plastic anisotropy for hexagonal close packed metals: Application to alloying effects on the formability of Mg. *J. Alloys Compd.* **2017**, *695*, 1488–1497. [CrossRef]
13. Suh, B.C.; Kim, J.H.; Hwang, J.H.; Shim, M.S.; Kim, N.J. Twinning-mediated formability in Mg alloys. *Sci. Rep.* **2016**, *6*, 22364. [CrossRef] [PubMed]
14. Simkin, B.A.; Ng, B.C.; Crimp, M.A.; Bieler, T.R. Crack opening due to deformation twin shear at grain boundaries in near-γ TiAl. *Intermetallics* **2007**, *15*, 55–60. [CrossRef]
15. Yang, F.; Yin, S.M.; Li, S.X.; Zhang, Z.F. Crack initiation mechanism of extruded AZ31 magnesium alloy in the very high cycle fatigue regime. *Mater. Sci. Eng. A* **2008**, *491*, 131–136. [CrossRef]
16. Yin, S.M.; Yang, F.; Yang, X.M.; Wu, S.D.; Li, S.X.; Li, G.Y. The role of twinning–detwinning on fatigue fracture morphology of Mg–3%Al–1%Zn alloy. *Mater. Sci. Eng. A* **2008**, *1–2*, 397–400. [CrossRef]
17. Kumar, M.A.; Beyerlein, I.J. Local microstructure and micromechanical stress evolution during deformation twinning in hexagonal polycrystals. *J. Mater. Res.* **2020**, *35*, 217–241. [CrossRef]
18. Beyerlein, I.J.; Tomé, C.N. A probabilistic twin nucleation model for HCP polycrystalline metals. *Proc. R. Soc. Lond. Ser. A* **2010**, *466*, 2517–2544. [CrossRef]
19. Khosravani, A.; Fullwood, D.T.; Adams, B.L.; Rampton, T.M.; Miles, M.P.; Mishra, R.K. Nucleation and propagation of $\{10\bar{1}2\}$ twins in AZ31 magnesium alloy. *Acta Mater.* **2015**, *100*, 202–214. [CrossRef]
20. Wang, J.; Beyerlein, I.J.; Tomé, C.N. An atomic and probabilistic perspective on twin nucleation in Mg. *Scr. Mater.* **2010**, *63*, 741–746. [CrossRef]
21. Wang, J.; Beyerlein, I.J.; Tomé, C.N. Reactions of lattice dislocations with grain boundaries in Mg: Implications on the micro scale from atomic-scale calculations. *Int. J. Plast.* **2014**, *56*, 156–172. [CrossRef]
22. Wang, J.; Yadav, S.K.; Hirth, J.P.; Tomé, C.N.; Beyerlein, I.J. Pure-shuffle nucleation of deformation twins in hexagonal-close-packed metals. *Mater. Res. Lett.* **2013**, *1*, 126–132. [CrossRef]
23. Yu, Q.; Qi, L.; Chen, K.; Mishra, R.K.; Li, J.; Minor, A.M. The nanostructured origin of deformation twinning. *Nano Lett.* **2012**, *12*, 887–892. [CrossRef] [PubMed]
24. Hu, Y.; Turlo, V.; Beyerlein, I.J.; Mahajan, S.; Lavernia, E.J.; Schoenung, J.M.; Rupert, T.J. Disconnection-mediated twin embryo growth in Mg. *Acta Mater.* **2020**, *194*, 437–451. [CrossRef]
25. Jiang, L.; Gong, M.; Wang, J.; Pan, Z.; Wang, X.; Zhang, D.; Wang, Y.M.; Ciston, J.; Minor, A.M.; Xu, M.; et al. Visualization and validation of twin nucleation and early-stage growth in magnesium. *Nat. Commun.* **2022**, *13*, 20. [CrossRef]
26. Paudel, Y.; Giri, D.; Priddy, M.W.; Barrett, C.D.; Inal, K.; Tschopp, M.A.; Rhee, H.; El Kadiri, H. A review on capturing twin nucleation in crystal plasticity for hexagonal metals. *Metals* **2021**, *11*, 1373. [CrossRef]

27. Kumar, M.A.; Wroński, M.; McCabe, R.J.; Capolungo, L.; Wierzbanowski, K.; Tomé, C.N. Role of microstructure on twin nucleation and growth in HCP titanium: A statistical study. *Acta Mater.* **2018**, *148*, 123–132. [CrossRef]
28. Kumar, M.A.; Kanjarla, A.K.; Niezgoda, S.R.; Lebensohn, R.A.; Tomé, C.N. Numerical study of the stress state of a deformation twin in magnesium. *Acta Mater.* **2015**, *84*, 349–358. [CrossRef]
29. Yaghoobi, M.; Chen, Z.; Murphy-Leonard, A.D.; Sundararaghavan, V.; Daly, S.; Allison, J.E. Deformation twinning and detwinning in extruded Mg-4Al: In-situ experiment and crystal plasticity simulation. *Int. J. Plast.* **2022**, *155*, 103345. [CrossRef]
30. Kumar, M.A.; Beyerlein, I.J. Influence of plastic properties on the grain size effect on twinning in Ti and Mg. *Mater. Sci. Eng. A* **2020**, *771*, 138644. [CrossRef]
31. Kumar, M.A.; Beyerlein, I.J.; Tomé, C.N. Grain size constraints on twin expansion in hexagonal close packed crystals. *J. Appl. Phys.* **2016**, *120*, 155105. [CrossRef]
32. Song, H.y.; Li, Y.l. Effect of twin boundary spacing on deformation behavior of nanotwinned magnesium. *Phys. Lett. A* **2012**, *376*, 529–533. [CrossRef]
33. Paudel, Y.; Indeck, J.; Hazeli, K.; Priddy, M.W.; Inal, K.; Rhee, H.; Barrett, C.D.; Whittington, W.R.; Limmer, K.R.; El Kadiri, H. Characterization and modeling of $\{10\bar{1}2\}$ twin banding in magnesium. *Acta Mater.* **2020**, *183*, 438–451. [CrossRef]
34. Della Ventura, N.M.; Kalacska, S.; Casari, D.; Edwards, T.E.; Sharma, A.; Michler, J.; Logé, R.; Maeder, X. $\{10\bar{1}2\}$ twinning mechanism during in situ micro-tensile loading of pure Mg: Role of basal slip and twin-twin interactions. *Mater. Des.* **2021**, *197*, 109206. [CrossRef]
35. Russell, W.D.; Bratton, N.R.; Paudel, Y.; Moser, R.D.; McClelland, Z.B.; Barrett, C.D.; Oppedal, A.L.; Whittington, W.R.; Rhee, H.; Mujahid, S.; et al. In situ characterization of the effect of twin-microstructure interactions on $\{10\bar{1}2\}$ tension and $\{10\bar{1}1\}$ contraction twin nucleation, growth and damage in magnesium. *Metals* **2020**, *10*, 1403. [CrossRef]
36. Barrett, C.D.; El Kadiri, H. The roles of grain boundary dislocations and disclinations in the nucleation of $\{10\bar{1}2\}$ twinning. *Acta Mater.* **2014**, *63*, 1–15. [CrossRef]
37. Barrett, C.D.; El Kadiri, H. Impact of deformation faceting on $\{10\bar{1}2\}$,$\{10\bar{1}1\}$ and $\{10\bar{1}3\}$ embryonic twin nucleation in hexagonal close-packed metals. *Acta Mater.* **2014**, *70*, 137–161. [CrossRef]
38. Ostapovets, A.; Gröger, R. Twinning disconnections and basal–prismatic twin boundary in magnesium. *Model. Simul. Mater. Sci. Eng.* **2014**, *22*, 025015. [CrossRef]
39. Ostapovets, A.; Molnár, P. On the relationship between the "shuffling-dominated" and "shear-dominated" mechanisms for $\{10\bar{1}2\}$ twinning in magnesium. *Scr. Mater.* **2013**, *69*, 287–290. [CrossRef]
40. Vaidya, S.; Mahajan, S. Accommodation and formation of $\{11\bar{2}1\}$ twins in Co single crystals. *Acta Metall.* **1980**, *28*, 1123–1131. [CrossRef]
41. Dubertret, A.; Le Lann, A. Development of a new model for atom movement in twinning. Case of the $\{10\bar{1}1\}$, $\{10\bar{1}3\}$ twins and $\{10\bar{1}1\}\{10\bar{1}2\}$ double twinning in H.C.P. metals. *Phys. Status Solidi (a)* **1980**, *60*, 145–151. [CrossRef]
42. Braisaz, T.; Ruterana, P.; Nouet, G.; Pond, R.C. Investigation of {1012} twins in Zn using high-resolution electron microscopy: Interfacial defects and interactions. *Philos. Mag. A* **1997**, *75*, 1075–1095. [CrossRef]
43. Giri, D.; ElKadiri, H.; Limmer, K.R.; Barrett, C.D. An atomistic gateway into capturing twin nucleation in crystal plasticity. *Philos. Mag. Lett.* **2020**, *100*, 375–385. [CrossRef]
44. Zhou, N.; Zhang, G.; Guo, T.F.; Guo, X.; Tang, S.; Huang, X. Twin nucleation at prismatic/basal boundary in hexagonal close-packed metals. *Philos. Mag.* **2019**, *99*, 2584–2603. [CrossRef]
45. Jiang, L.; Radmilović, V.R.; Sabisch, J.E.; Qi, L.; Minor, A.M.; Chrzan, D.C.; Asta, M. Twin nucleation from a single $\langle c+a \rangle$ dislocation in hexagonal close-packed crystals. *Acta Mater.* **2021**, *202*, 35–41. [CrossRef]
46. Ostapovets, A.; Serra, A. Slip dislocation and twin nucleation mechanisms in hcp metals. *J. Mater. Sci.* **2017**, *52*, 533–540. [CrossRef]
47. Li, J.; Li, X.; Yu, M.; Sui, M. Nucleation mechanism of $\{101\ 2\}$ twin with low Schmid factor in hexagonal close-packed metals. *Mater. Sci. Eng. A* **2020**, *791*, 139542. [CrossRef]
48. Morrow, B.M.; McCabe, R.J.; Cerreta, E.K.; Tomé, C.N. Observations of the atomic structure of tensile and compressive twin boundaries and twin–twin interactions in zirconium. *Metall. Mater. Trans. A* **2014**, *45*, 5891–5897. [CrossRef]
49. Ostapovets, A.; Serra, A. Characterization of the matrix–twin interface of a $(10\bar{1}2)$ twin during growth. *Philos. Mag.* **2014**, *94*, 2827–2839. [CrossRef]
50. Sun, Q.; Zhang, X.Y.; Tu, J.; Ren, Y.; Qin, H.; Liu, Q. Characterization of basal-prismatic interface of twin in deformed titanium by high-resolution transmission electron microscopy. *Philos. Mag. Lett.* **2015**, *95*, 145–151. [CrossRef]
51. Huang, Z.; Turlo, V.; Wang, X.; Chen, F.; Shen, Q.; Zhang, L.; Beyerlein, I.J.; Rupert, T.J. Dislocation-induced Y segregation at basal-prismatic interfaces in Mg. *Comput. Mater. Sci.* **2021**, *188*, 110241. [CrossRef]
52. Wang, X.; Hu, Y.; Yu, K.; Mahajan, S.; Beyerlein, I.J.; Lavernia, E.J.; Rupert, T.J.; Schoenung, J.M. Room temperature deformation-induced solute segregation and its impact on twin boundary mobility in a Mg-Y alloy. *Scr. Mater.* **2022**, *209*, 114375. [CrossRef]
53. Somekawa, H.; Basha, D.A.; Singh, A.; Tsuru, T.; Watanabe, H. Change in damping capacity arising from twin-boundary segregation in solid-solution magnesium alloys. *Philos. Mag. Lett.* **2020**, *100*, 494–505. [CrossRef]
54. Liu, C.; Shanthraj, P.; Diehl, M.; Roters, F.; Dong, S.; Dong, J.; Ding, W.; Raabe, D. An integrated crystal plasticity–phase field model for spatially resolved twin nucleation, propagation, and growth in hexagonal materials. *Int. J. Plast.* **2018**, *106*, 203–227. [CrossRef]

55. Serra, A.; Bacon, D.J. A new model for 1012 twin growth in hcp metals. *Philos. Mag. A* **1996**, *73*, 333–343. [CrossRef]
56. Nie, J.F.; Zhu, Y.M.; Liu, J.Z.; Fang, X.Y. Periodic segregation of solute atoms in fully coherent twin boundaries. *Science* **2013**, *340*, 957–960. [CrossRef]
57. Zhao, X.; Chen, H.; Wilson, N.; Liu, Q.; Nie, J.F. Direct observation and impact of co-segregated atoms in magnesium having multiple alloying elements. *Nat. Commun.* **2019**, *10*, 3243. [CrossRef]
58. Tang, J.; Fan, H.; Wei, D.; Jiang, W.; Wang, Q.; Tian, X.; Zhang, X. Interaction between a $\{10\bar{1}2\}$ twin boundary and grain boundaries in magnesium. *Int. J. Plast.* **2020**, *126*, 102613. [CrossRef]
59. Abdolvand, H.; Daymond, M.R. Multi-scale modeling and experimental study of twin inception and propagation in hexagonal close-packed materials using a crystal plasticity finite element approach—Part I: Average behavior. *J. Mech. Phys. Solids* **2013**, *61*, 783–802. [CrossRef]
60. Abdolvand, H.; Daymond, M.R.; Mareau, C. Incorporation of twinning into a crystal plasticity finite element model: Evolution of lattice strains and texture in Zircaloy-2. *Int. J. Plast.* **2011**, *27*, 1721–1738. [CrossRef]
61. Abdolvand, H.; Majkut, M.; Oddershede, J.; Wright, J.P.; Daymond, M.R. Study of 3-D stress development in parent and twin pairs of a hexagonal close-packed polycrystal: Part II – crystal plasticity finite element modeling. *Acta Mater.* **2015**, *93*, 235–245. [CrossRef]
62. Abdolvand, H.; Wright, J.; Wilkinson, A.J. Strong grain neighbour effects in polycrystals. *Nat. Commun.* **2018**, *9*, 171. [CrossRef] [PubMed]
63. Kumar, M.A.; Beyerlein, I.J.; Lebensohn, R.A.; Tomé, C.N. Modeling the effect of neighboring grains on twin growth in HCP polycrystals. *Model. Simul. Mater. Sci. Eng.* **2017**, *25*, 064007. [CrossRef]
64. Kumar, M.A.; Beyerlein, I.J.; Tomé, C.N. Effect of local stress fields on twin characteristics in HCP metals. *Acta Mater.* **2016**, *116*, 143–154. [CrossRef]
65. Kumar, M.A.; Beyerlein, I.J.; Lebensohn, R.A.; Tomé, C.N. Role of alloying elements on twin growth and twin transmission in magnesium alloys. *Mater. Sci. Eng. A* **2017**, *706*, 295–303. [CrossRef]
66. Herrera-Solaz, V.; Hidalgo-Manrique, P.; Pérez-Prado, M.T.; Letzig, D.; Llorca, J.; Segurado, J. Effect of rare earth additions on the critical resolved shear stresses of magnesium alloys. *Mater. Lett.* **2014**, *128*, 199–203. [CrossRef]
67. Kim, K.H.; Jeon, J.B.; Kim, N.J.; Lee, B.J. Role of yttrium in activation of $\langle c+a \rangle$ slip in magnesium: An atomistic approach. *Scr. Mater.* **2015**, *108*, 104–108. [CrossRef]
68. Tsuru, T.; Chrzan, D.C. Effect of solute atoms on dislocation motion in Mg: An electronic structure perspective. *Sci. Rep.* **2015**, *5*, 8793. [CrossRef]
69. Wang, J.; Wang, X.; Yu, K.; Rupert, T.J.; Mahajan, S.; Lavernia, E.J.; Schoenung, J.M.; Beyerlein, I.J. Manipulating deformation mechanisms with Y alloying of Mg. *Mater. Sci. Eng. A* **2021**, *817*, 141373. [CrossRef]
70. Maldar, A.; Wang, L.; Zhu, G.; Zeng, X. Investigation of the alloying effect on deformation behavior in Mg by Visco-Plastic Self-Consistent modeling. *J. Magnes. Alloys* **2020**, *8*, 210–218. [CrossRef]
71. Jiang, L.; Kumar, M.A.; Beyerlein, I.J.; Wang, X.; Zhang, D.; Wu, C.; Cooper, C.; Rupert, T.J.; Mahajan, S.; Lavernia, E.J.; et al. Twin formation from a twin boundary in Mg during in-situ nanomechanical testing. *Mater. Sci. Eng. A* **2019**, *759*, 142–153. [CrossRef]
72. Paudel, Y.; Barrett, C.D.; Tschopp, M.A.; Inal, K.; El Kadiri, H. Beyond initial twin nucleation in hcp metals: Micromechanical formulation for determining twin spacing during deformation. *Acta Mater.* **2017**, *133*, 134–146. [CrossRef]
73. Moulinec, H.; Suquet, P. A numerical method for computing the overall response of nonlinear composites with complex microstructure. *Comput. Methods Appl. Mech. Eng.* **1998**, *157*, 69–94. [CrossRef]
74. Brenner, R.; Lebensohn, R.A.; Castelnau, O. Elastic anisotropy and yield surface estimates of polycrystals. *Int. J. Solids Struct.* **2009**, *46*, 3018–3026. [CrossRef]
75. Lebensohn, R.A. N-site modeling of a 3D viscoplastic polycrystal using Fast Fourier Transform. *Acta Mater.* **2001**, *49*, 2723–2737. [CrossRef]
76. Lebensohn, R.A.; Brenner, R.; Castelnau, O.; Rollett, A.D. Orientation image-based micromechanical modelling of subgrain texture evolution in polycrystalline copper. *Acta Mater.* **2008**, *56*, 3914–3926. [CrossRef]
77. Lebensohn, R.A.; Idiart, M.I.; Castañeda, P.P.; Vincent, P.G. Dilatational viscoplasticity of polycrystalline solids with intergranular cavities. *Philos. Mag.* **2011**, *91*, 3038–3067. [CrossRef]
78. Lebensohn, R.A.; Kanjarla, A.K.; Eisenlohr, P. An elasto-viscoplastic formulation based on fast Fourier transforms for the prediction of micromechanical fields in polycrystalline materials. *Int. J. Plast.* **2012**, *32–33*, 59–69. [CrossRef]
79. Eisenlohr, P.; Diehl, M.; Lebensohn, R.A.; Roters, F. A spectral method solution to crystal elasto-viscoplasticity at finite strains. *Int. J. Plast.* **2013**, *46*, 37–53. [CrossRef]
80. Beyerlein, I.J.; McCabe, R.J.; Tomé, C.N. Effect of microstructure on the nucleation of deformation twins in polycrystalline high-purity magnesium: A multi-scale modeling study. *J. Mech. Phys. Solids* **2011**, *59*, 988–1003. [CrossRef]
81. Sudholz, A.; Gusieva, K.; Chen, X.; Muddle, B.; Gibson, M.; Birbilis, N. Electrochemical behaviour and corrosion of Mg–Y alloys. *Corros. Sci.* **2011**, *53*, 2277–2282.
82. Gu, X.; Li, N.; Zhou, W.; Zheng, Y.; Zhao, X.; Cai, Q.; Ruan, L. Corrosion resistance and surface biocompatibility of a microarc oxidation coating on a Mg–Ca alloy. *Acta Biomater.* **2011**, *7*, 1880–1889. [CrossRef]
83. Bakhsheshi-Rad, H.; Idris, M.; Abdul-Kadir, M.; Ourdjini, A.; Medraj, M.; Daroonparvar, M.; Hamzah, E. Mechanical and bio-corrosion properties of quaternary Mg–Ca–Mn–Zn alloys compared with binary Mg–Ca alloys. *Mater. Des.* **2014**, *53*, 283–292.

84. Zhang, Y.; Huo, Q.; Zhang, Z.; Xiao, Z.; Wang, C.; Hashimoto, A.; Yang, X. Effects of yttrium content on the three-dimensional compressive creep anisotropy of Mg-Y alloys. *Metall. Mater. Trans. A* **2021**, *52*, 3910–3930. [CrossRef]
85. Suzuki, M.; Sato, H.; Maruyama, K.; Oikawa, H. Creep deformation behavior and dislocation substructures of Mg–Y binary alloys. *Mater. Sci. Eng. A* **2001**, *319*, 751–755. [CrossRef]
86. Lupescu, S.; Istrate, B.; Munteanu, C.; Minciuna, M.G.; Focsaneanu, S.; Earar, K. Characterization of some master Mg-X System (Ca, Mn, Zr, Y) alloys used in medical applications. *Rev. Chim.* **2017**, *68*, 1408–1413. [CrossRef]
87. Simmons, G.; Wang, H. *Single Crystal Elastic Constants and Calculated Aggregate Properties: A Handbook*; MIT Press: Cambridge, MA, USA, 1971.
88. Ganeshan, S.; Shang, S.L.; Wang, Y.; Liu, Z.K. Effect of alloying elements on the elastic properties of Mg from first-principles calculations. *Acta Mater.* **2009**, *57*, 3876–3884. [CrossRef]
89. Luque, A.; Ghazisaeidi, M.; Curtin, W.A. A new mechanism for twin growth in Mg alloys. *Acta Mater.* **2014**, *81*, 442–456. [CrossRef]
90. Marian, J.; Cai, W.; Bulatov, V.V. Dynamic transitions from smooth to rough to twinning in dislocation motion. *Nat. Mater.* **2004**, *3*, 158–163. [CrossRef]
91. Hu, Y.; Turlo, V.; Beyerlein, I.; Mahajan, S.; Lavernia, E.; Schoenung, J.; Rupert, T. Embracing the chaos: Alloying adds stochasticity to twin embryo growth. *Phys. Rev. Lett.* **2020**, *125*, 205503. [CrossRef]
92. Morrow, B.M.; Cerreta, E.K.; McCabe, R.J.; Tomé, C.N. Toward understanding twin–twin interactions in hcp metals: Utilizing multiscale techniques to characterize deformation mechanisms in magnesium. *Mater. Sci. Eng. A* **2014**, *613*, 365–371. [CrossRef]